Synthesis of Core/Shell ZnO/rGO Nanoparticles by Calcination of ZIF-8/rGO Composites and Their Photocatalytic Activity

Batukhan Tatykayev, Florian Donat, Halima Alem, Lavinia Balan, Ghouti Medjahdid, Bolat Uralbekov, Raphael Schneider

ACS OMEGA

Article

http://pubs.acs.org/journal/acsodf

Synthesis of Core/Shell ZnO/rGO Nanoparticles by Calcination of ZIF-8/rGO Composites and Their Photocatalytic Activity

Batukhan Tatykayev,[†] Florian Donat,[‡] Halima Alem,[§] Lavinia Balan,[∥] Ghouti Medjahdi,[§] Bolat Uralbekov,[†] and Raphaël Schneider*[,‡]

[†]Al-Farabi Kazakh National University, Al-Farabi Avenue, 71, 050040 Almaty, Kazakhstan

[‡]Université de Lorraine, Laboratoire Réactions et Génie des Procédés (LRGP), UMR 7274, CNRS, 1 rue Grandville, BP 20451, 54001 Nancy Cedex, France

[§]Institut Jean Lamour (IJL), Université de Lorraine, CNRS, UMR 7198, CNRS, BP 70239, 54506 Vandoeuvre-lès-Nancy Cedex, France

[∥]Institut de Science des Matériaux de Mulhouse (IS2M), CNRS, UMR 7361, 15 rue Jean Starcky, 68093 Mulhouse, France

Supporting Information

ABSTRACT: A facile two-step method was developed to prepare core/shell ZnO/rGO particles from ZIF-8/rGO composites. ZIF-8 particles were first grown at the surface of rGO sheets. Next, ZIF-8 particles were transformed into ZnO particles by thermal decomposition under air at 500 °C. All materials were characterized by scanning electron microscopy, transmission electron microscopy, X-ray diffraction, Raman spectroscopy, thermogravimetric analysis, and Brunauer–Emmett–Teller analyses. Results obtained show that ZIF-8 particles strongly associate with rGO sheets and that the calcination of this material produces porous core/shell ZnO/rGO particles with an average diameter of ca. 40 nm. The wt % of rGO associated with ZIF-8 particles was varied from 5 to 20%. The ZnO/rGO (10%) particles exhibit the highest photocatalytic activity for the degradation of the Orange II dye under simulated solar light irradiation of weak intensity (5 mW/cm^2). This high photocatalytic activity was demonstrated to originate from superoxide $O_2^{\bullet-}$ radicals due to the efficient trapping of photogenerated electrons in ZnO by rGO.

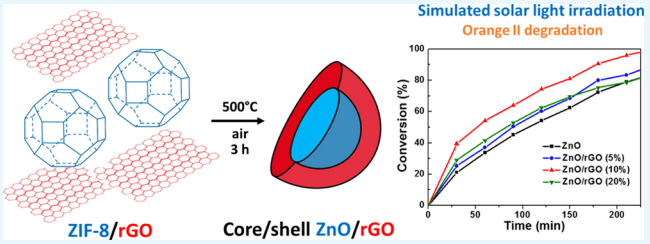

1. INTRODUCTION

ZIF-8 ($Zn(mim)_2$, mim^- = 2-methylimidazolate) is a zeolite-type metal organic framework possessing high chemical and thermal stabilities (up to 550 °C under nitrogen).[1−4] ZIF-8 particles exhibit the sodalite topology in which ZnN_4 tetrahedra are connected through mim^- linkers to form cages 1.16 nm in diameter and with an aperture size estimated to be 0.34 nm.[5,6] Owing to their high specific surface area (up to 1700 m^2/g) and pore volume (0.65 cm^3/g), ZIF-8 particles have found many applications, including selective adsorption,[7] separation,[8] sensing,[9] and catalysis.[10] ZIF-8 can also be used as a precursor for the preparation of porous materials. Calcination of ZIF-8 at a moderate temperature (400−500 °C) under air allows the preparation of ZnO,[11−15] whereas treatment at a higher temperature (900−1000 °C) yields nanoporous carbons.[16−19] A few studies have demonstrated that porous ZnO and carbons produced from ZIF-8 have high potential as a catalyst, as a photocatalyst, or for supercapacitor electrodes.[11,13,16,18]

Reduced graphene oxide (rGO) can be prepared by partial removal of epoxy, hydroxyl, and carboxylic acid functions from the edges and the basal planes of graphene oxide (GO). rGO has attracted high interest due to its electrical conductivity and high specific surface area compared to those of GO and has thus found promising applications in catalysis or drug delivery, as well as in devices like sensors and supercapacitors.[20−23]

Nanocomposites formed by metal oxides like ZnO and rGO have attracted great attention for photocatalytic applications due to the synergetic properties coming from each component.[24−32] ZnO/rGO photocatalysts have been demonstrated to be of high efficiency for the degradation of organic dyes like Methylene Blue under UV or artificial solar irradiation and for hydrogen production from water.[24−32]

ZnO is one of the leading photocatalysts for water treatment due to its high photosensitivity, its ability to generate reactive oxygen species, its low cost, and its weak toxicity.[33−37] Upon light excitation, electron/hole pairs in ZnO may react with oxygen and water to generate superoxide ($O_2^{\bullet-}$) and hydroxyl ($^{\bullet}OH$) radicals that allow the oxidation of various organic compounds in air or in water. If ZnO is well associated with rGO, rGO will not only act as a sink of the photogenerated electrons but will also allow their migration and thus hinder the charge recombination and improve the photocatalytic efficiency.

Received: May 25, 2017
Accepted: August 11, 2017
Published: August 24, 2017

DOI: 10.1021/acsomega.7b00673
ACS Omega 2017, 2, 4946−4954

Scheme 1. Schematic Representation of the Synthetic Route Used for the Preparation of ZIF-8/rGO Composites and Their Conversion into ZnO/rGO Particles by Calcination

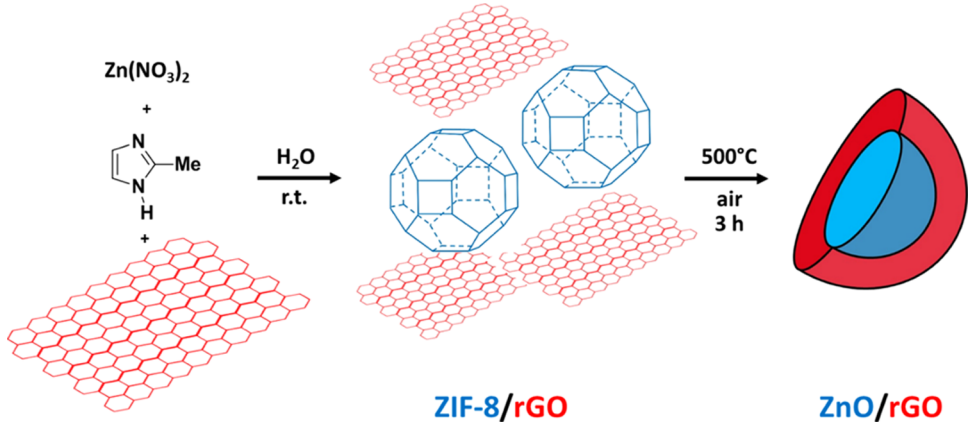

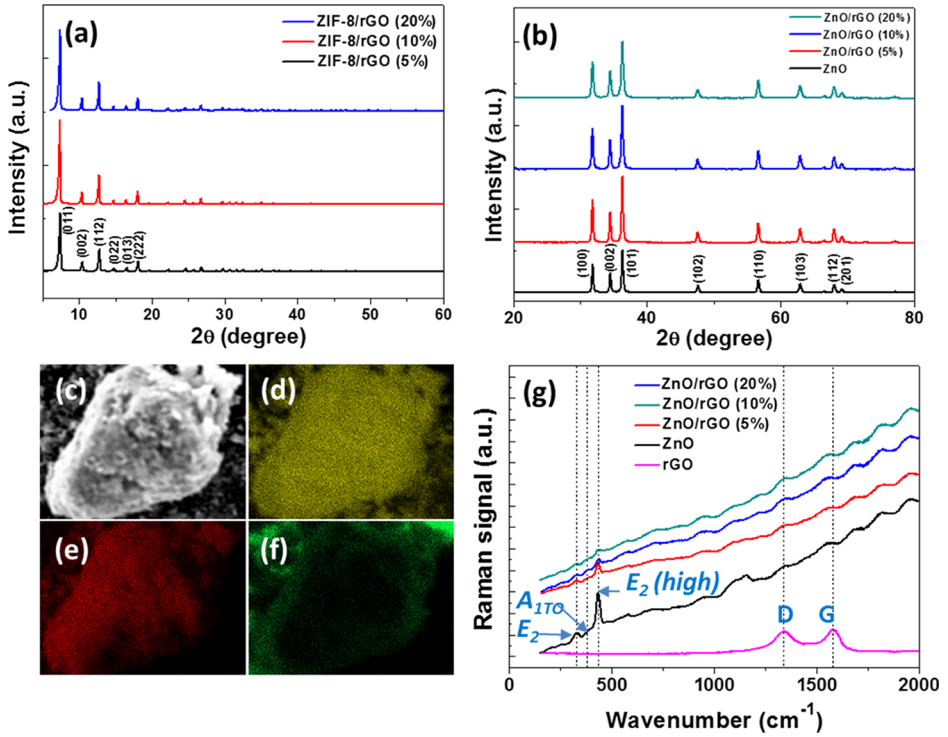

Figure 1. XRD patterns of (a) ZIF-8/rGO composites when varying the rGO content (5, 10, and 20 wt %) and (b) ZnO and ZnO/rGO particles. (c) SEM image of ZnO/rGO (10%) particles. EDX elemental mapping of the ZnO/rGO particles showing the presence of (d) Zn, (e) O, and (f) C elements. (g) Raman spectra of rGO, ZnO, and ZnO/rGO particles.

In this article, we report the first synthesis of ZIF-8/rGO nanocomposites and their successful transformation into core/shell ZnO/rGO particles by annealing at 500 °C. ZnO particles have an average diameter of 40 nm and are capped by a continuous rGO shell with a thickness of ca. 5 nm. The use of ZnO/rGO materials as photocatalysts for the degradation of the Orange II dye under simulated solar light was also explored.

2. RESULTS AND DISCUSSION

2.1. Synthesis and Structure of ZnO/rGO Particles. A simple two-step method was developed to prepare core/shell ZnO/rGO particles using ZIF-8/rGO composites as precursors (Scheme 1). Briefly, ZIF-8 particles were produced by reacting $Zn(NO_3)_2$ with Hmim in water in the presence of rGO sheets to form ZIF-8/rGO composites.[38,39] Next, ZnO/rGO particles were prepared by thermal decomposition of ZIF-8/rGO composites at 500 °C and under air.

The evolutions of morphology, crystalline structure, optical properties, and texture during the thermal decomposition of ZIF-8/rGO composites into ZnO/rGO particles were investigated by X-ray diffraction (XRD), scanning electron microscopy (SEM), transmission electron microscopy (TEM), diffuse reflectance spectroscopy, Raman spectroscopy, and Brunauer–Emmett–Teller (BET) analyses. Powder XRD patterns of ZIF-8/rGO composites with rGO contents of 5, 10, and 20 wt % are similar to those of pure ZIF-8,[4] indicating that the sodalite structure of ZIF-8 crystals was not altered by association with rGO (Figure 1a). The weak and broad diffraction peak of rGO at $2\theta = 25°$ could not be observed in all of the samples prepared. An SEM image of rGO shows crumpled sheets, which is the typical morphology of

DOI: 10.1021/acsomega.7b00673
ACS Omega 2017, 2, 4946−4954

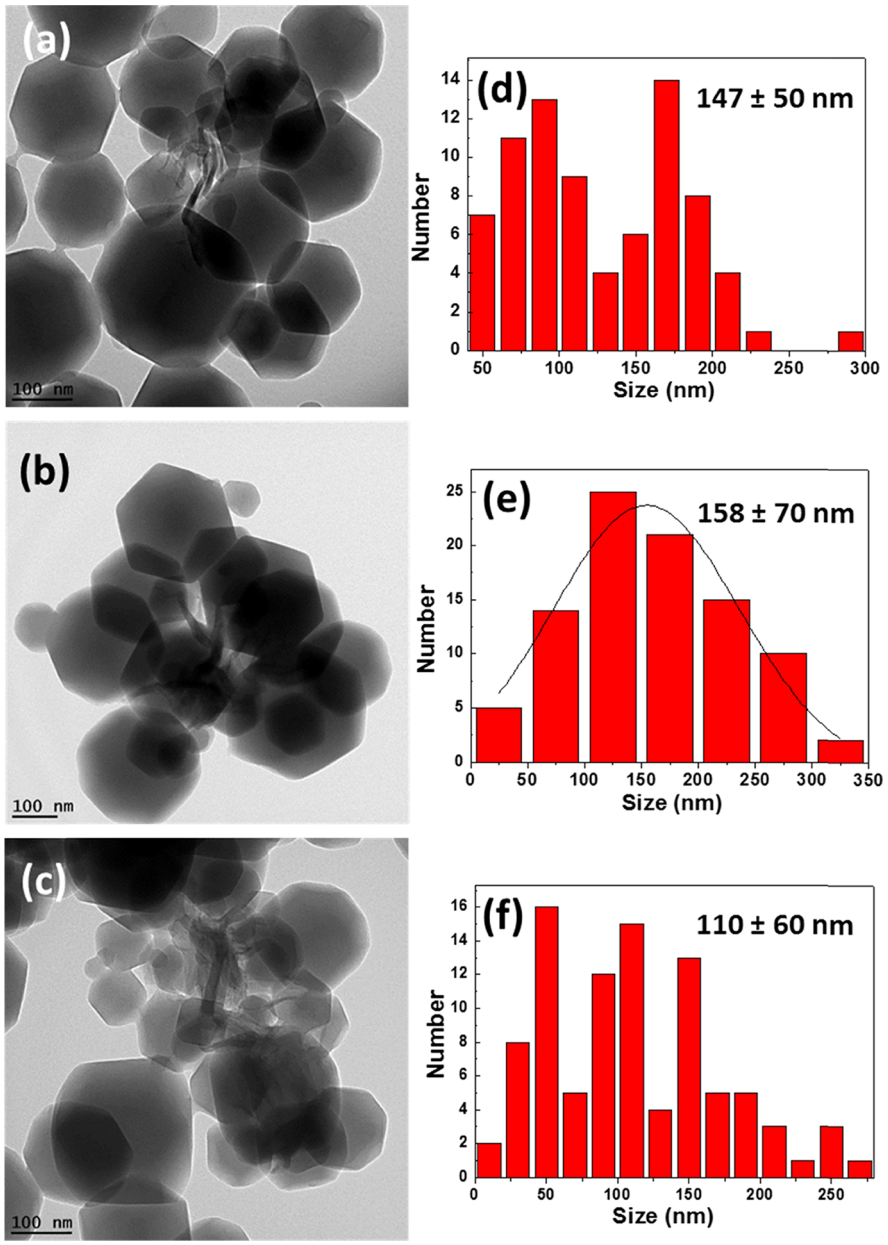

Figure 2. TEM images of (a) ZIF-8/rGO (5%), (b) ZIF-8/rGO (10%), and (c) ZIF-8/rGO (20%) composites and (d–f) the corresponding size distributions.

rGO (Figure S1a). SEM images demonstrate that ZIF-8 crystals were strongly associated with rGO sheets, suggesting that ZIF-8 crystals nucleate and grow around rGO due to the coordination of Zn^{2+} cations with hydroxyl and carboxylate functions present at the surface of rGO sheets (Figure S1b–d). This is in accordance with a previous report related to the preparation of ZIF-8/GO composites.[40] The strong association of ZIF-8 crystals with rGO was further confirmed by TEM (Figure 2). For rGO contents of 5 and 10 wt %, most of the ZIF-8 particles exhibit the typical rhombic dodecahedron morphology (Figure 2a,b).[4] The largest ZIF-8 particles have an average diameter of ca. 225 nm, and no significant changes in particles sizes and distributions and in morphology were detected between these two samples (the average diameters are 147 ± 50 and 158 ± 70 nm for ZIF-8 particles associated with 5 and 10% rGO, respectively). For the composite prepared with 20 wt % rGO, more particles with irregular or spherical morphology could be observed along with smaller ones (Figure 2c). The estimated average diameter (110 ± 60 nm) indicates that a high amount of rGO in the reaction medium perturbs the growth of ZIF-8 crystals.

After a thermal treatment at 500 °C for 3 h, ZIF-8/rGO composites transform into core/shell ZnO/rGO particles. All the diffraction peaks of these materials can be indexed to the standard hexagonal wurtzite structure of ZnO (space group $P6_3mc$, JCPDS No 36-1451) and were sharp, indicating the high crystallinity of ZnO produced by the thermal decomposition of ZIF-8 (Figure 1b). As previously observed for ZIF-8/rGO composites, rGO was not detected by XRD analyses.

The association of rGO with ZnO was demonstrated using energy dispersive X-ray spectroscopy (EDX). The C element was present besides Zn and O, and the elemental mapping indicates that rGO was homogeneously distributed at the surface of ZnO particles (Figure 1c–f). The C element was not detected by the

DOI: 10.1021/acsomega.7b00673
ACS Omega 2017, 2, 4946–4954

elemental mapping at the surface of ZnO particles produced from ZIF-8 (Figure S2), indicating that pure ZnO is produced after the calcination at 500 °C and that the mim^- linker decomposition does not generate any carbon-based materials. This result is in accordance with previous reports.[11,12] The wurtzite structure of ZnO was further confirmed by Raman spectroscopy (Figure 1g). The signals located at 329, 373, and 432 cm^{-1} can be assigned to the E_2, A_{1TO}, and E_2 (high) vibration modes of ZnO, respectively. The D and G bands of starting rGO were observed at 1339 and 1583 cm^{-1}, respectively. The I_D/I_G ratio is 1.07, indicating that rGO is of high graphitic degree. Only weak signals were detected for the D and G bands after calcination, although Raman spectroscopy is highly versatile for the characterization of graphitic materials,[41] suggesting that the structure of rGO was markedly altered during the conversion of ZIF-8 into ZnO particles.

The changes in rGO morphology during the calcination step were confirmed by TEM and HR-TEM (Figure 3). ZnO particles

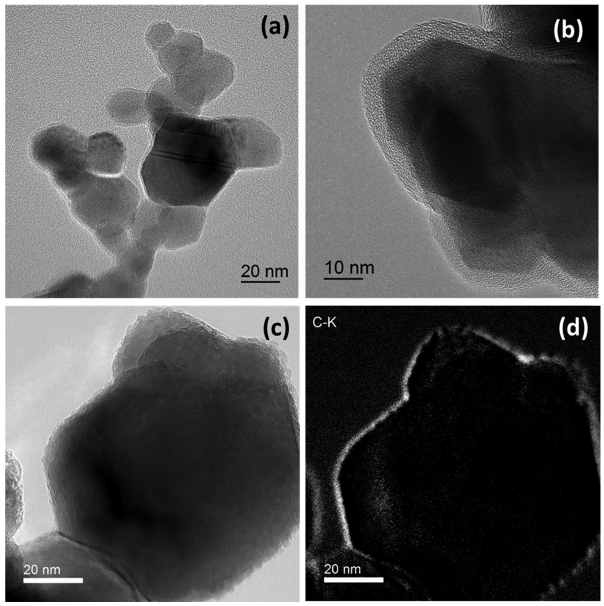

Figure 3. (a) TEM image and (b, c) HR-TEM images of the ZnO/rGO (10%) particles and (d) the C-mapping corresponding to image (c).

produced from ZIF-8 have an average diameter of 40 ± 10 nm, are of spherical/ellipsoidal morphology, and are covered by a smooth and continuous rGO shell with a thickness of ca. 5 nm (see Figure 3a,b for the ZnO/rGO (10%) sample). HR-TEM and the corresponding C-mapping conducted with Energy Filtered-TEM (EF-TEM) demonstrate that an rGO layer uniformly surrounds ZnO crystals, yielding core/shell ZnO/rGO particles (Figure 3c,d). This shell could not be observed at the periphery of ZnO particles produced after calcination of ZIF-8 crystals (Figure S3), which is in good agreement with the EDX elemental mapping shown in Figure S2.

The thermal stability of the ZIF-8/rGO (10%) composite was compared to that of pure ZIF-8 crystals by thermogravimetric analyses. Under an O_2 atmosphere, ZIF-8 particles start to decompose at ca. 400 °C into ZnO, and the weight loss observed is 65%.[4] Under N_2, a weak weight loss of ca. 7%, corresponding to the desorption of surface-bound water and/or the removal of guest molecules like Hmim, was observed between 20 and 200 °C (Figure 4a). The ZIF-8 framework exhibits higher stability under N_2 than under O_2, and its gradual decomposition occurs

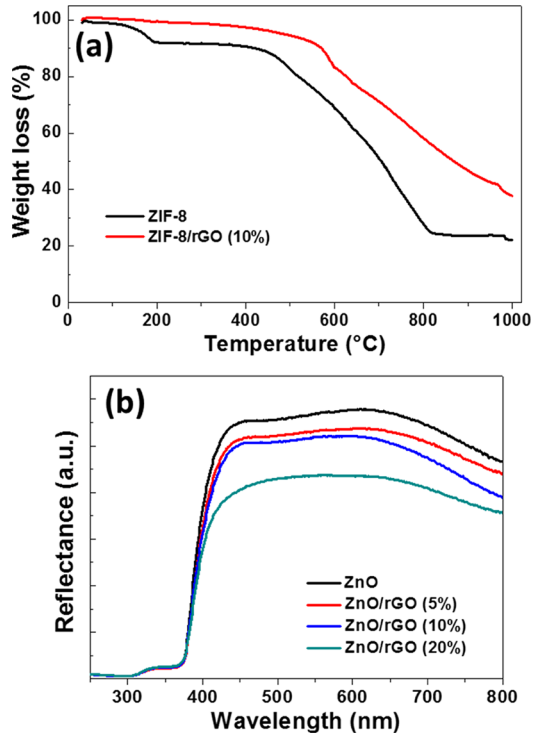

Figure 4. (a) Thermogravimetric profiles of ZIF-8 and ZIF-8/rGO (10%) composites in a nitrogen atmosphere and (b) UV−visible diffuse reflectance spectra of ZnO and ZnO/rGO particles.

between 450 and 800 °C, leaving ca. 25 wt % of nanoporous carbon as the residue.[17] The thermal stability of the ZIF-8/rGO (10%) composite under N_2 is increased compared to that of pure ZIF-8 particles. A long quasiplateau is observed in the temperature range of 20−550 °C. A marked weight loss (ca. 62%) related to the decomposition of the mim^- linker occurs from 550 to 1000 °C. By comparing the weight loss of ZIF-8 and ZIF-8/rGO, the actual content of rGO in the composite can be estimated to be 13%, a value only slightly higher than the theoretical content in rGO (10%). This result further demonstrates than the ZIF-8 crystal nucleation and growth are only weakly perturbed by the presence of 10 wt % rGO.

The UV−visible diffuse reflectance spectra of ZnO/rGO particles are shown in Figure 4b. The absorption edge of ZnO is located at ca. 370 nm, which corresponds to a bandgap of 3.25 eV using the Tauc model $\alpha h\nu \sim (h\nu - E_g)^{1/2}$, where α is the absorption coefficient, h is the Planck's constant, ν is the frequency of vibration, and E_g is the bandgap. The bandgap of ZnO particles remains unchanged after association with rGO. However, due to the relatively high absorption coefficient of rGO in the visible region, the absorbance of core/shell ZnO/rGO particles increases in this wavelength region with the increase of rGO content. ZnO/rGO particles will harvest more light than ZnO and should exhibit an enhanced photocatalytic activity under simulated solar light irradiation.

The specific surface area, pore size, and pore size distributions were determined by N_2 adsorption and desorption isotherms (Figure 5). ZIF-8/rGO composites exhibit typical type-IV adsorption isotherms according to the IUPAC classification (Figure 5a).[42] A first steep increase of N_2 adsorption at a low relative pressure ($P/P_0 < 0.1$) and a slight increase at a high relative pressure ($P/P_0 > 0.9$) are indicative of the microporosity of the composites. A second step can be observed at $P/P_0 = 0.05$,

DOI: 10.1021/acsomega.7b00673
ACS Omega 2017, 2, 4946−4954

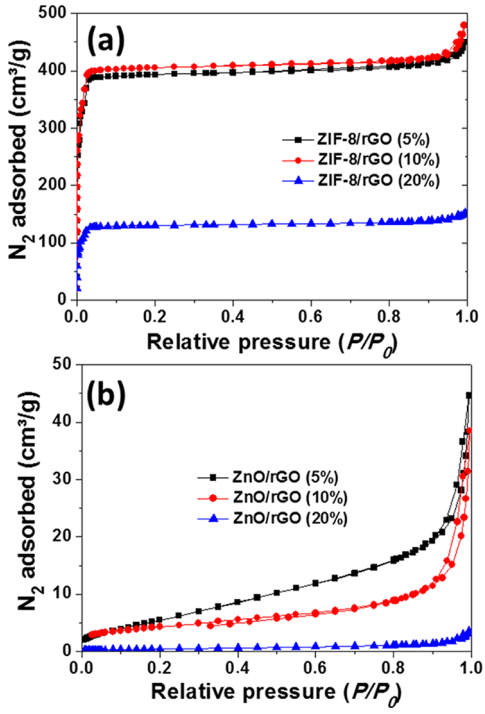

Figure 5. Nitrogen adsorption−desorption isotherms of (a) ZIF-8/rGO composites and (b) ZnO/rGO particles.

which probably originates from mesoporous rGO. The specific surface areas, determined using the Brunauer−Emmett−Teller (BET) method, the pore size, and the pore volume of ZIF-8/rGO (5 and 10%) composites are listed in Table 1 and are in good agreement with those measured for pure ZIF-8 crystals.[1,4] The BET results show that the surface area decreases when a high amount of rGO (20 wt %) is combined with ZIF-8 crystals, suggesting a strong association of ZIF-8 with rGO and that the cavities inside ZIF-8 are partially blocked by rGO sheets. After thermolysis, the microporous network collapsed but mesopores and micropores were still present in the ZnO/rGO (5 and 10%) particles as demonstrated by N_2 adsorption and desorption isotherms (Figure 5b). The fast increase of the material isotherms at relative P/P_0 near 1 is close to type III isotherms[42] and suggests also the presence of macropores.

Table 1. BET Specific Surface Areas, Pore Sizes, and Pore Volumes Determined for ZIF-8/rGO and ZnO/rGO Materials

material	specific surface (m^2/g)	pore size (nm)	pore volume (cm^3/g)
ZIF-8/rGO (5%)	1774 ± 68	1.34	0.69
ZIF-8/rGO (10%)	1771 ± 32	1.37	0.74
ZIF-8/rGO (20%)	562 ± 8	1.37	0.23
ZnO/rGO (5%)	24 ± 0.6	34.9	0.07
ZnO/rGO (10%)	15 ± 0.1	44.4	0.06
ZnO/rGO (20%)	1 ± 0.1	38.5	0.005

2.2. Photocatalytic Activity. ZnO and ZnO/rGO particles produced from ZIF-8 and ZIF-8/rGO composites, respectively, were evaluated for the photocatalytic degradation of aqueous solutions of the Orange II dye (10 mg/L) at pH = 7 and under simulated solar light irradiation (intensity = 5 mW/cm^2). The Orange II diazo dye was selected as a model pollutant because it has no photosensitizing activity, contrary to Methylene Blue or Rhodamine that promote the photodegradation process. No changes were observed in the Orange II UV−visible absorption spectra in control experiments conducted in the dark in the presence of the photocatalyst. Similar results were obtained under light irradiation in the absence of the photocatalyst, indicating that the photoinduced self-degradation of the dye does not occur. After stirring in the dark for 60 min, the adsorption capacity of ZnO/rGO (10%) particles (24%) is slightly higher than that of ZnO or ZnO/rGO (5 or 20%) particles (17%) (Figure 6a). As can be seen, the degree of Orange II photodegradation varied with the content of rGO associated with ZnO. An increase of rGO content from 5 to 10 wt % increased the photocatalytic activity, probably because electrons are more efficiently captured and thus electron/hole pair recombinations are reduced. Nearly 99% of the dye was bleached in 240 min using the ZnO/rGO (10%) catalyst. The decrease in photocatalytic activity observed for ZnO/rGO (20%) particles may be ascribed to the increased light absorption and scattering of this material due to its darker color compared to that of ZnO/rGO (5 and 10%) particles. This result is consistent with previous studies.[31]

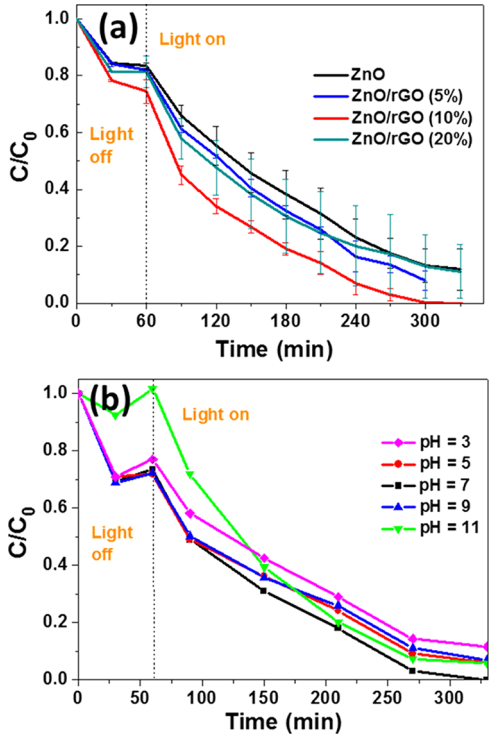

Figure 6. (a) Influence of the rGO loading on the photocatalytic activity of ZnO/rGO nanoparticles for the degradation of Orange II in aqueous solution at pH = 7. (b) Influence of pH on the photodegradation of Orange II by the ZnO/rGO (10%) composite (C is the Orange II concentration at time t, and C_0 is the concentration of the dye at t = 0; volume of solution, 40 mL; Orange II concentration, 10 mg/L).

The photodegradation kinetics of Orange II could be fitted to a pseudo-first-order reaction $\ln(C/C_0) = -kt$, where C_0 is the initial concentration of the dye, C is the concentration at time t, and k is the degradation rate constant (min^{-1}). Using the fitting results described in Figure S4, the k values determined from the slopes of the straight lines are 0.007, 0.008, 0.013, and 0.007 min^{-1} for ZnO and for the ZnO/rGO particles with rGO loadings of 5, 10, and 20%, respectively. These values confirm that the synergetic

DOI: 10.1021/acsomega.7b00673
ACS Omega 2017, 2, 4946−4954

effect between ZnO and rGO is optimal when using 10 wt % of rGO relative to ZnO.

The pH of the aqueous solution does not play a key role in the photocatalytic efficiency of ZnO/rGO particles (Figure 6b). The adsorption of the dye on the photocatalyst surface was not affected by pH changes from 3 to 9. The degradation rate is the highest at pH = 7 (k = 0.013 min^{-1}). The k values determined at pH = 3, 5, and 9 are lower (0.007, 0.007, and 0.006 min^{-1}, respectively), but no detrimental effect on the photodegradation was observed (Figure S5). At pH = 11, no adsorption of Orange II at the surface of the catalyst was observed, but the further oxidation of the dye proceeded efficiently (k = 0.011 min^{-1}). The point of zero charge of the ZnO/rGO catalyst was determined to be 7.7, a value lower than that of pure ZnO (pzc = 9.0 ± 0.3)[43] due to the presence of rGO at the periphery of ZnO particles (the pzc of pure rGO is 3.5 ± 0.4). For Orange II, the pK_a of the naphthol function is 11.4 and the sulfonic acid is present in its sulfonate form in the whole pH range studied (pK_a = 1). It is therefore likely that Orange II is only repelled by the ZnO/rGO catalyst at high pH values but without consequences on the photodegradation. At lower pH values, Orange II probably binds to the ZnO/rGO particle surface through hydrogen bonds (naphthol with Zn−OH at pH values lower than 7.7 or naphthol with Zn−O$^-$ at pH values higher than 7.7). ZnO is well-known to exhibit a higher photocatalytic activity at basic pH (the optimal activity is generally located at pHs 9−10),[43] which was ascribed to the easier production of hydroxyl radicals $^\bullet$OH from $^-$OH than from H_2O. For the ZnO/rGO photocatalyst, the highest activity was observed at neutral pH, which may be linked to the presence of rGO at the surface of ZnO.

We also evaluated the stability of the photocatalyst after the reaction conducted at pHs 3, 7, and 11. The photocatalysts were recovered by centrifugation after the Orange II photodegradations and their structure analyzed by XRD. No changes in the XRD patterns were observed compared to those of the native ZnO/rGO particles (Figure S6), indicating that ZnO did not dissolve or decompose even in strong alkaline or acidic aqueous solution. This high stability of ZnO/rGO particles may be attributed to the rGO shell surrounding and protecting the ZnO core from the environment.

2.3. Mechanism of the Photodegradation. The photocatalytic activity of a material depends among others on its specific surface area, and thus its adsorption capability, as well as on the effectiveness of photogenerated electrons and holes separation. We compared the dark adsorption of Orange II at the surface of ZnO and ZnO/rGO (10%) particles. A slight increase of the dye adsorption from 19 to 24% was observed when rGO was associated with ZnO (Figure S7). This result demonstrates that the adsorption capacity does not play a key role on the improved photocatalytic activity of ZnO/rGO particles and more likely originates from the effective photogenerated electron transfer from ZnO to rGO deposited at its surface.

Orange II may be photodegraded by $^\bullet$OH and $O_2^{\bullet-}$ radicals and holes (h^+) generated after activation of the ZnO/rGO catalyst by light. Trapping experiments were conducted using t-BuOH, ammonium oxalate, p-benzoquinone, and $K_2S_2O_8$ as $^\bullet$OH, h^+, $O_2^{\bullet-}$, and e^- scavengers, respectively. Figure 7a and the related pseudo-first-order kinetic plots (Figure S8) demonstrate that p-benzoquinone had the most deleterious effect (k = 0.002 min^{-1}), indicating that $O_2^{\bullet-}$ radicals are the main oxidative species responsible for the degradation of the dye, probably because rGO promotes the e^- delocalization and their reaction with O_2. This was further proved by conducting the photodegradation in an N_2-saturated solution (Figure 7b). It can be seen that the photodegradation rate was decreased in the N_2-saturated solution (k = 0.0066 min^{-1}) compared to that in the air-equilibrated solution (k = 0.013 min^{-1}) (Figure S9). $^\bullet$OH radicals and direct oxidation of the dye by h^+ are also involved in the mechanism but to a lesser extent than $O_2^{\bullet-}$ (k = 0.005 and 0.004 min^{-1} for reactions conducted in the presence of t-BuOH and ammonium oxalate, respectively) (Figure 7a). Finally, the e^- scavenger, $K_2S_2O_8$, does not quite have an effect (k = 0.012 vs 0.013 min^{-1} in the absence of a scavenger), suggesting that e^- photogenerated and then trapped by rGO quickly react with O_2 to yield $O_2^{\bullet-}$ radicals.

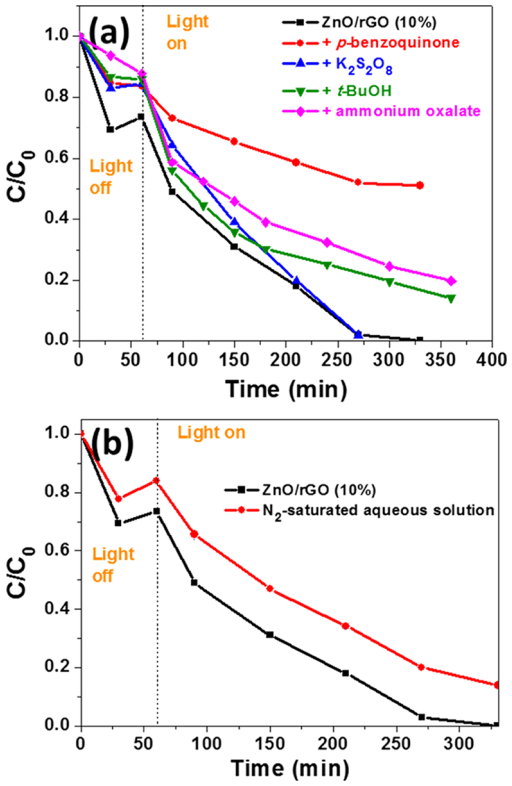

Figure 7. (a) Influence of t-BuOH, p-benzoquinone, $K_2S_2O_8$, and ammonium oxalate used as $^\bullet$OH, $O_2^{\bullet-}$, e^-, and h^+ scavengers, respectively, on the photocatalytic activity of ZnO/rGO particles. Except p-benzoquinone used at 0.1 mM, all scavengers were used at a 10 mM concentration. (b) Photocatalytic degradation of Orange II in air-equilibrated (black line) and N_2-purged (red line) aqueous solutions.

Using the bandgap of ZnO determined from UV−visible absorption spectra (E_g = 3.25 eV), the band edge positions of the valence (VB) and of the conduction band (CB) of ZnO were determined using the Mulliken electronegativity theory.[44]

$$E_{VB} = \chi - E_c + \frac{1}{2}E_g \quad (1)$$

$$E_{CB} = E_{VB} - E_g \quad (2)$$

where χ is the absolute electronegativity of ZnO (5.89 eV) and E_c is the energy of free electrons on a hydrogen scale (4.5 eV). Using eqs 1 and 2, the E_{VB} and E_{CB} of ZnO were estimated to be 2.915 and −0.335 eV, respectively (Figure 8a). The Fermi level of rGO is −0.08 eV versus NHE.[45] Thus, e^- can easily be transferred from the ZnO CB to rGO before reacting with O_2 to form $O_2^{\bullet-}$ radicals (the potential of rGO being more negative than that of the $O_2/O_2^{\bullet-}$ couple, −0.046 eV). Holes in the VB of ZnO have a

DOI: 10.1021/acsomega.7b00673
ACS Omega 2017, 2, 4946−4954

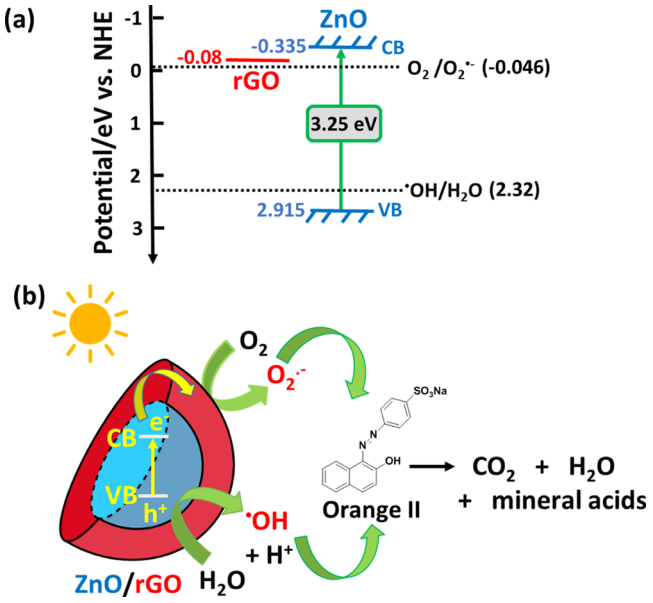

Figure 8. (a) Energy levels of ZnO and rGO and redox potentials of $O_2/O_2^{\bullet-}$ and $^{\bullet}OH/H_2O$ couples. (b) Schematic representation of the solar light photocatalytic activity of core/shell ZnO/rGO particles.

potential greater than 2.32 eV and are able to generate $^{\bullet}OH$ radicals. On the basis of trapping experiments and on the well-coupled energy levels of ZnO, rGO, and the $O_2/O_2^{\bullet-}$ and $H_2O/^{\bullet}OH$ couples, it can be concluded that the photocatalytic activity is mainly governed by the separation efficiency of e^- and h^+. Once ZnO is excited by solar light, e^- are efficiently transferred to rGO due to the core/shell structure of ZnO/rGO particles that will promote the transport of e^- and h^+ across ZnO particles due to the dipolar fields originating from charged surface domains.[46] These e^- quickly react with O_2 and generate $O_2^{\bullet-}$ radicals. In the meanwhile, the h^+ in the VB of ZnO oxidize H_2O to yield $^{\bullet}OH$ radicals (H^+ is the by-product) or the dye (Figure 8b).

3. CONCLUSIONS

In conclusion, a simple method allowing the preparation of new core/shell ZnO/rGO particles using ZIF-8 as the precursor of ZnO was developed. We first demonstrated that ZIF-8 particles can successfully be grown in an aqueous solution at the surface of rGO sheets. Next, rGO sheets were found to deposit at the periphery of ZnO particles during the calcination of ZIF-8, yielding core/shell ZnO/rGO particles with an average diameter of 40 nm. At low rGO loading (5 or 10 wt %), the high specific surface of ZIF-8 is maintained (S_{BET} = 1700 m^2/g) and is partly transferred to ZnO during the calcination. ZnO/rGO (10%) particles exhibit the highest photocatalytic activity for the degradation of the Orange II dye under simulated solar light irradiation. The mechanism of the photodegradation was studied, and the key role played by superoxide $O_2^{\bullet-}$ radicals was demonstrated, indicating the ability of the rGO shell to trap the photogenerated electrons in ZnO. Our study should open the way for engineering new metal oxide/rGO core/shell particles of high interest for catalytic or sensing applications by simply varying the MOF used as the precursor.

4. EXPERIMENTAL SECTION

4.1. Materials. Graphite powder (Merck), $KMnO_4$ (>99%, Sigma), $Zn(NO_3)_2{\cdot}6H_2O$ (>98%, Sigma), 2-methylimidazole (Hmim, Sigma), H_2O_2 (30%, VWR Chemicals), $KMnO_4$ (>99%, Sigma), $NaNO_3$ (>99%, Sigma), sulfuric acid (reagent grade), L-ascorbic acid (reagent grade, Sigma), *tert*-butanol (>99.5%, Sigma), *p*-benzoquinone (>98%, Sigma), potassium peroxodisulfate (>99%, Sigma), ammonium oxalate (>99%, Sigma), sodium hydroxide (>97%, Sigma), and ethanol were used as received without further purification. All solutions were prepared using Milli-Q water (18.2 MΩ cm, Millipore) as the solvent.

4.2. Preparation of Exfoliated Graphene Oxide (GO). GO was prepared by oxidation of graphite by a modified Hummer's method, followed by exfoliation.[47] In brief, 2 g of graphite and 1 g of $NaNO_3$ were mixed in a flask kept at 0 °C. Then, 50 mL of concentrated H_2SO_4 was added dropwise, and the mixture was stirred for 30 min. $KMnO_4$ (0.3 g) was added to the solution, and the mixture was stirred for 30 min. Next, 7 g of $KMnO_4$ was added portion-wise, and the mixture was further stirred for 1 h at a temperature below 20 °C. Then, the temperature was increased to 35 °C. After 2 h, 90 mL of H_2O was slowly added (the temperature increased to ca. 70 °C), and the mixture was stirred for 15 min, followed by the addition of a mixture of 7 mL of H_2O_2 and 55 mL of water to reduce the residual $KMnO_4$ to soluble manganese ions. Next, the suspension was filtered using a polycarbonate membrane, washed 4 times with 5% aqueous HCl and 5 times with water. GO was obtained as a brownish powder after drying at 60 °C for 24 h. This powder was dispersed in water (1 mg/mL), and the exfoliation was conducted by ultrasonication for 1 h by probe sonication (amplitude 25%). Finally, GO was collected by centrifugation (5000 rpm for 15 min) and dried at 60 °C for 24 h before use.

4.3. Reduction of GO. The reduction of GO into rGO was conducted according to the procedure described by Zhang et al.[48] with slight modifications. Briefly, 15 mg of GO was dispersed by sonication in 50 mL of water. L-Ascorbic acid (200 mg) was added to the GO dispersion, and the mixture was stirred at room temperature for 24 h. rGO was collected by centrifugation (4000 rpm for 15 min), washed with water, and dried overnight at 60 °C.

4.4. Synthesis of ZIF-8/rGO Nanocomposites. The ZIF-8 precursor was prepared accordingly to procedures reported in the literature with slight modifications.[38,39] A typical synthesis for the ZIF-8/rGO (10%) composite is described. Briefly, 12.3 g of Hmim were dissolved in 90 mL of water. Next, 50 mg of rGO was added to the Hmim solution, and the mixture was sonicated for 10 min to obtain a homogeneous solution. Under stirring, to the Hmim and rGO solution was added 0.744 g of $Zn(NO_3)_2{\cdot}6H_2O$ in 10 mL of water, and the solution was further stirred for 15 h at room temperature. The ZIF-8/rGO composite was recovered from the solution by centrifugation (4000 rpm for 15 min) and washed one time with water and two times with ethanol. The product was dried in an oven for 2 h at 70 °C. ZIF-8/rGO (5%) and ZIF-8/rGO (20%) composites were prepared using the same synthetic protocol except that 25 and 100 mg of rGO were used, respectively.

4.5. Preparation of ZnO/rGO Particles. The ZIF-8/rGO composite was placed in a ceramic boat and then transferred to a furnace. The calcination was performed at 500 °C (heating rate of 10 °C/min) for 3 h under air. The ZnO/rGO particles were isolated as gray powders after cooling to room temperature and used without treatment for photocatalytic studies.

4.6. Photocatalytic Performance Test. The photocatalytic activity of ZnO/rGO particles for the degradation of Orange II (10 mg/L in water) was evaluated by recording the UV−visible absorption of the solution after illumination. The simulated solar

DOI: 10.1021/acsomega.7b00673
ACS Omega 2017, 2, 4946−4954

light was generated by Sylvania LuxLine FHO T5 neon tubes. The light intensity at the surface of the Orange II solution was 5 mW/cm^2. In a typical experiment, ZnO/rGO particles (40 mg) were dispersed in 40 mL of the Orange II aqueous solution. Before irradiation, the suspension was magnetically stirred in the dark under ambient conditions for 1 h to attain the adsorption−desorption equilibrium. Samples were taken at regular time intervals and immediately centrifuged (4000 rpm for 2 min) to remove the ZnO/rGO photocatalyst. The quantity of dye in the aqueous solution was determined by measuring the absorption intensity of Orange II at 485 nm.

To investigate the active species photoproduced during the degradation process, experiments were conducted using *tert*-butanol (*t*-BuOH, 10 mM), *p*-benzoquinone (0.1 mM), potassium peroxodisulfate ($K_2S_2O_8$, 10 mM), and ammonium oxalate ($(NH_4)_2C_2O_4$, 10 mM) as scavengers of $^{\bullet}OH$ and $O_2^{\bullet-}$ free radicals, electrons, and holes, respectively.

4.7. Instruments and Characterization. TEM studies were conducted with a JEOL ARM 200F-Cold FEG TEM/STEM. HR-TEM imaging was performed with a JEOL ARM 200F-Cold FEG fitted with a GIF Quantum ER. Electron energy loss spectroscopy experiments were recorded in the scanning transmission electron microscopy (STEM) mode. The EF-TEM images were recorded in the STEM mode. For each sample, one drop of particles dispersed in ethanol was deposited on holey carbon grids and imaged. SEM pictures were recorded using a JEOL JSM-6490 LV Microscope. The element mapping of the ZnO/rGO photocatalyst was detected by EDX analysis. Crystal phases of samples were identified using an X'Pert MPD diffractometer with Cu Kα radiation (λ = 0.15418 nm). The specific surface areas, pore sizes, and pore volumes of the samples were characterized by N_2 absorption using a Micromeritics 3Flex Surface Characterization Analyzer instrument. Before the analyses, the samples were out-gassed overnight under primary vacuum at 40 °C, followed by 4 h out-gassing under high vacuum. Data were analyzed using the Brunauer−Emmett−Teller (BET) method, and the micropore volume (V_{micro}) was determined using the Horvath−Kawazoe equation. The ζ potential of ZnO/rGO particles was determined using a Malvern Zetasizer Nano ZS equipment. The thermal stabilities of the samples were analyzed using a TGA STA 449 F3 Jupiter equipment (Netzsch), and acquisitions were conducted from 20 to 1000 °C with a heating rate of 10 °C/min.

All of the optical measurements were performed at room temperature under ambient conditions. UV−visible absorption spectra of liquid samples were recorded on a Thermo Scientific Evolution 220 spectrophotometer. UV−visible DR spectra were recorded on a Shimadzu 2600 spectrophotometer within the wavelength range of 250−1400 nm. $BaSO_4$ powder was used as a standard for baseline measurements. Raman spectra were acquired using a Horiba Scientific Xplora spectrometer at an excitation wavelength of 532 nm.

■ ASSOCIATED CONTENT

Supporting Information

The Supporting Information is available free of charge on the ACS Publications website at DOI: 10.1021/acsomega.7b00673.

SEM images, EDX elemental mapping, TEM and HR-TEM images, first-order kinetic plots, XRD patterns, and UV−visible absorption spectra related to photocatalytic studies (PDF)

■ AUTHOR INFORMATION

Corresponding Author

*E-mail: raphael.schneider@univ-lorraine.fr. Tel: +33 3 83 17 50 53.

ORCID

Raphaël Schneider: 0000-0002-6870-6902

Notes

The authors declare no competing financial interest.

■ ACKNOWLEDGMENTS

This work is supported by the Agence Nationale pour la Recherche (ANR CD2I 2013, project PRUMOS). The authors also thank the Kazakhstan Ministry of Education and Science program 0130/PTSF-14 for its financial support.

■ REFERENCES

(1) Park, K. S.; Ni, Z.; Côté, A. P.; Choi, J. Y.; Huang, R. D.; Uribe-Romo, F. J.; Chae, H. K.; O'Keeffe, M.; Yaghi, O. M. Exceptional Chemical and Thermal Stability of Zeolitic Imidazolate Frameworks. *Proc. Natl. Acad. Sci. U.S.A.* **2006**, *103*, 10186−10191.

(2) Küsgens, P.; Rose, M.; Senkovska, I.; Fröde, H.; Henschel, A.; Siegle, S.; Kaskel, S. Crystal Growth of the Metal-Organic Framework $Cu_3(BTC)_2$ on the Surface of Pulp Fibers. *Microporous Mesoporous Mater.* **2009**, *120*, 325−330.

(3) Cychosz, K. A.; Matzger, A. Water Stability of Microporous Coordination Polymers and the Adsorption of Pharmaceuticals from Water. *Langmuir* **2010**, *26*, 17198−17202.

(4) Schejn, A.; Balan, L.; Falk, V.; Aranda, L.; Medjahdi, G.; Schneider, R. Fe_3O_4@ZIF-8: Controlling ZIF-8 Nano- and Microcrystal Formation and Reactivity Through Zinc Salt Variations. *CrystEngComm* **2014**, *16*, 4493−4500.

(5) Wang, B.; Côté, A. P.; Furukawa, H.; O'Keeffe, M.; Yaghi, O. M. Colossal Cages in Zeolitic Imidazolate Frameworks as Selective Carbon Dioxide Reservoirs. *Nature* **2008**, *453*, 207−211.

(6) Banerjee, R.; Phan, A.; Wang, B.; Knobler, C.; Furukawa, H.; O'Keeffe, M.; Yaghi, O. M. High-Throughput Synthesis of Zeolitic Imidazolate Frameworks and Application to CO_2 Capture. *Science* **2008**, *319*, 939−943.

(7) Kumari, G.; Jayaramulu, K.; Maji, T. K.; Narayana, C. Temperature Induced Structural Transformations and Gas Adsorption in the Zeolitic Imidazolate Framework ZIF-8: a Raman Study. *J. Phys. Chem. A* **2013**, *117*, 11006−11012.

(8) Bux, H.; Chmelik, C.; Krishna, R.; Caro, J. Ethene/Ethane Separation by the MOF Membrane ZIF-8: Molecular Correlation of Permeation, Adsorption, Diffusion. *J. Membr. Sci.* **2011**, *369*, 284−289.

(9) Lu, G.; Hupp, J. T. Metal-Organic Frameworks as Sensors: a ZIF-8 Based Fabry-Pérot Device as a Selective Sensor for Chemical Vapors and Gases. *J. Am. Chem. Soc.* **2010**, *132*, 7832−7833.

(10) Schejn, A.; Mazet, T.; Falk, V.; Balan, L.; Aranda, L.; Medjahdi, G.; Schneider, R. Fe_3O_4@ZIF-8: Magnetically Recoverable Catalysts by Loading Fe_3O_4 Nanoparticles Inside a Zinc Imidazolate Framework. *Dalton Trans.* **2015**, *44*, 10136−10140.

(11) Du, Y.; Chen, R. Z.; Yao, J. F.; Wang, H. T. Facile Fabrication of Porous ZnO by Thermal Treatment of Zeolitic Imidazolate Framework-8 and its Photocatalytic Activity. *J. Alloys Compd.* **2013**, *551*, 125−130.

(12) Wee, L. H.; Janssens, N.; Sree, S. P.; Wiktor, C.; Gobechiya, E.; Fischer, R. A.; Kirschhock, C. E. A.; Martens, J. A. Local Transformation of ZIF-8 Powders and Coatings into ZnO Nanorods for Photocatalytic Application. *Nanoscale* **2014**, *6*, 2056−2060.

(13) He, L.; Li, L.; Wang, T.; Gao, H.; Li, G.; Wu, X.; Su, Z.; Wang, C. Fabrication of Au/ZnO Nanoparticles Derived from ZIF-8 with Visible Light Photocatalytic Hydrogen Production and Degradation Dye Activities. *Dalton Trans.* **2014**, *43*, 16981−16985.

(14) Khaletskaya, K.; Turner, S.; Tu, M.; Wannapalboon, S.; Scheemann, A.; Meyer, R.; Ludwig, A.; Tendeloo, G. V.; Fischer, R. A.

DOI: 10.1021/acsomega.7b00673
ACS Omega 2017, 2, 4946−4954

Self-Directed Localization of ZIF-8 Thin Film Formation by Conversion of ZnO Nanolayers. *Adv. Funct. Mater.* **2014**, *24*, 4804−4811.
(15) Cao, X.; Zeng, B.; Rui, X.; Shi, W.; Yan, Q.; Zhang, H. Metal Oxide-Coated Three-Dimensional Graphene Prepared by the Use of Metal-Organic Frameworks as Precursors. *Angew. Chem., Int. Ed.* **2014**, *53*, 1404−1409.
(16) Chaikittisilp, W.; Hu, M.; Wang, H.; Huang, H.-S.; Fujita, T.; Wu, K. C.-W.; Chen, L.-C.; Yamauchi, Y.; Ariga, K. Nanoporous Carbons Through Direct Carbonization of a Zeolitic Imidazolate Framework for Supercapacitor Electrodes. *Chem. Commun.* **2012**, *48*, 7259−7261.
(17) Torad, N. L.; Hu, M.; Kamachi, Y.; Takai, K.; Imura, M.; Naito, M.; Yamauchi, Y. Facile Synthesis of Nanoporous Carbons with Controlled Particle Sizes by Direct Carbonization of Monodispersed ZIF-8 Crystals. *Chem. Commun.* **2013**, *49*, 2521−2523.
(18) Zhang, L.; Su, Z.; Jiang, F.; Yang, L.; Qian, J.; Zhou, Y.; Li, W.; Hong, M. Highly Graphitized Nitrogen-doped Porous Carbon Nanopolyhedra Derived from ZIF-8 Nanocrystals as Efficient Electrocatalysts for Oxygen Reduction Reactions. *Nanoscale* **2014**, *6*, 6590−6602.
(19) Zhong, H.-x.; Wang, J.; Zhang, Y.-w.; Xu, W.-L; Xing, W.; Xu, D.; Zhang, Y.-f.; Zhang, X.-b. ZIF-8 Derived Graphene-based Nitrogen-doped Porous Carbon Sheets as Highly Efficient and Durable Oxygen Reduction Electrocatalysts. *Angew. Chem., Int. Ed.* **2014**, *53*, 14235−14239.
(20) Eda, G.; Franchini, G.; Chrowalla, M. Large-area Ultrathin Films of Reduced Graphene Oxide as a Transparent and Flexible Electronic Material. *Nat. Nanotechnol.* **2008**, *3*, 270−271.
(21) Compton, O. C.; Nguyen, S. T. Graphene Oxide, Highly Reduced Graphene Oxide, and Graphene: Versatile Building Blocks for Carbon-based Materials. *Small* **2010**, *6*, 711−723.
(22) Dreyer, D. R.; Park, S.; Bielawski, C. W.; Ruoff, R. S. The Chemistry of Graphene Oxide. *Chem. Soc. Rev.* **2010**, *39*, 228−240.
(23) Pei, S.; Cheng, H.-M. The Reduction of Graphene Oxide. *Carbon* **2012**, *50*, 3210−3228.
(24) Akhavan, O. Graphene Nanomesh by ZnO Nanorod Photocatalysts. *ACS Nano* **2010**, *4*, 4174−4180.
(25) Lv, T.; Pan, L.; Liu, X.; Lu, T.; Zhu, G.; Sun, Z. Enhanced Photocatalytic Degradation of Methylene Blue by ZnO-reduced Graphene Oxide Composite Synthesized via Microwave-assisted Reaction. *J. Alloys Compd.* **2011**, *509*, 10086−10091.
(26) Lv, T.; Pan, L.; Liu, X.; Sun, Z. Enhanced Photocatalytic Degradation of Methylene Blue by ZnO-Reduced Graphene Oxide−Carbon Nanotube Composites Synthesized via Microwave-Assisted Reaction. *Catal. Sci. Technol.* **2012**, *2*, 2297−2301.
(27) Zhou, X.; Shi, T.; Zhou, H. Hydrothermal Preparation of ZnO-Reduced Graphene Oxide Hybrid with High Performance in Photocatalytic Degradation. *Appl. Surf. Sci.* **2012**, *258*, 6204−6211.
(28) Tien, H. N.; Luan, V. H.; Hoa, L. T.; Khoa, N. T.; Hahn, S. H.; Chung, J. S.; Shin, E. W.; Hur, S. H. One-pot Synthesis of a Reduced Graphene Oxide-Zinc Oxide Sphere Composite and its Use as a Visible Light Photocatalyst. *Chem. Eng. J.* **2013**, *229*, 126−133.
(29) Sun, H.; Liu, S.; Liu, S.; Wang, S. A Comparative Study of Reduced Graphene Oxide Modified TiO_2, ZnO and Ta_2O_5 in Visible Light Photocatalytic/Photochemical Oxidation of Methylene Blue. *Appl. Catal., B* **2014**, *146*, 162−168.
(30) Pawar, R. C.; Lu, C. S. Single-Step Sensitization of Reduced Graphene Oxide Sheets and CdS Nanoparticles on ZnO Nanorods as Visible-Light Photocatalysts. *Appl. Catal., B* **2014**, *144*, 57−65.
(31) Moussa, H.; Girot, E.; Mozet, K.; Alem, H.; Medjahdi, G.; Schneider, R. ZnO Rods/Reduced Graphene Oxide Composites Prepared via a Solvothermal Reaction for Efficient Sunlight-Driven Photocatalysis. *Appl. Catal., B* **2016**, *185*, 11−21.
(32) Kang, W.; Jimeng, X.; Xitao, W. The Effects of ZnO Morphology on Photocatalytic Efficiency of ZnO/RGO nanocomposites. *Appl. Surf. Sci.* **2016**, *360*, 270−275.
(33) Hariharan, C. Photocatalytic Degradation of Organic Contaminants in Water by ZnO Nanoparticles: Revisited. *Appl. Catal., A* **2006**, *304*, 55−61.
(34) Tian, C.; Zhang, Q.; Wu, A.; Jiang, M.; Liang, Z.; Jiang, B.; Fu, H. Cost-Effective Large-Scale Synthesis of ZnO Photocatalyst with Excellent Performance for Dye Photodegradation. *Chem. Commun.* **2012**, *48*, 2858−2860.
(35) Luo, Q.-P.; Yu, X.-Y.; Lei, B.-X.; Chen, H.-Y.; Kuang, D.-B.; Su, C.-Y. Reduced Graphene Oxide-Hierarchical ZnO Hollow Sphere Composites with Enhanced Photocurrent and Photocatalytic Activity. *J. Phys. Chem. C* **2012**, *116*, 8111−8117.
(36) Chouchene, B.; Ben Chaabane, T.; Balan, L.; Girot, E.; Mozet, K.; Medjahdi, G.; Schneider, R. High Performance Ce-doped ZnO Nanorods for Sunlight-Driven Photocatalysis. *Beilstein J. Nanotechnol.* **2016**, *7*, 1338−1349.
(37) Achouri, F.; Corbel, S.; Balan, L.; Mozet, K.; Girot, E.; Medjahdi, G.; Ben Said, M.; Ghrabi, A.; Schneider, R. Porous Mn-doped ZnO Nanoparticles for Enhanced Solar and Visible Light Photocatalysis. *Mater. Des.* **2016**, *101*, 309−316.
(38) Tanaka, S.; Kida, K.; Okita, M.; Ito, Y.; Miyake, Y. Size-Controlled Synthesis of Zeolitic Imidazolate Framework-8 (ZIF-8) Crystals in an Aqueous System at Room Temperature. *Chem. Lett.* **2012**, *41*, 1337−1339.
(39) Kida, K.; Okita, M.; Fujita, K.; Tanaka, S.; Miyake, Y. Formation of High Crystalline ZIF-8 in an Aqueous Solution. *CrystEngComm* **2013**, *15*, 1794−1801.
(40) Kumar, R.; Jayaramulu, K.; Maji, T. K.; Rao, C. N. R. Hybrid Nanocomposites of ZIF-8 with Graphene Oxide Exhibiting Tunable Morphology, Significant CO_2 Uptake and other Novel Properties. *Chem. Commun.* **2013**, *49*, 4947−4949.
(41) Ferrari, A. C.; Basko, D. M. Raman Spectroscopy as a Versatile Tool for Studying the Properties of Graphene. *Nat. Nanotechnol.* **2013**, *8*, 235−246.
(42) Sing, K. S. W. Reporting Physisorption Data for Gas/Solid Systems with Special Reference to the Determination of Surface Area and Porosity. *Pure Appl. Chem.* **1985**, *57*, 603−619.
(43) Sakthivel, S.; Neppolian, B.; Shankar, M. V.; Arabindoo, B.; Palanichamy, M.; Murugesan, V. Solar Photocatalytic Degradation of Azo Dye: Comparison of Photocatalytic Efficiency of ZnO and TiO_2. *Sol. Energy Mater. Sol. Cells* **2003**, *77*, 65−82.
(44) Xu, Y.; Schoonen, M. A. A. The Absolute Energy Positions of Conduction and Valence Bands of Selected Semiconducting Minerals. *Am. Mineral.* **2000**, *85*, 543−556.
(45) Yang, N.; Zhai, J.; Wang, D.; Chen, Y. S.; Jiang, L. Two-Dimensional Graphene Bridges Enhanced Photoinduced Charge Transport in Dye-Sensitized Solar Cells. *ACS Nano* **2010**, *4*, 887−894.
(46) Chen, D.; Wang, K.; Xiang, D.; Zong, R.; Yao, W.; Zhu, Y. Study on the Separation Mechanisms of Photogenerated Electrons and Holes for Composite Photocatalysts g-C_3N_4-WO_3. *Appl. Catal., B* **2014**, *147*, 554−561.
(47) Wang, K.; Ruan, J.; Song, H.; Zhang, J.; Wo, Y.; Guo, S.; Cui, D. Biocompatibility of Graphene Oxide. *Nanoscale Res. Lett.* **2011**, *6*, 8.
(48) Zhang, J.; Yang, H.; Shen, G.; Cheng, P.; Zhang, J.; Guo, S. Reduction of Graphene Oxide via L-Ascorbic Acid. *Chem. Commun.* **2010**, *46*, 1112−1114.

DOI: 10.1021/acsomega.7b00673
ACS Omega 2017, 2, 4946−4954